J. Fluid Mech. (2023), *vol*. 974, A43, doi:10.1017/jfm.2023.852

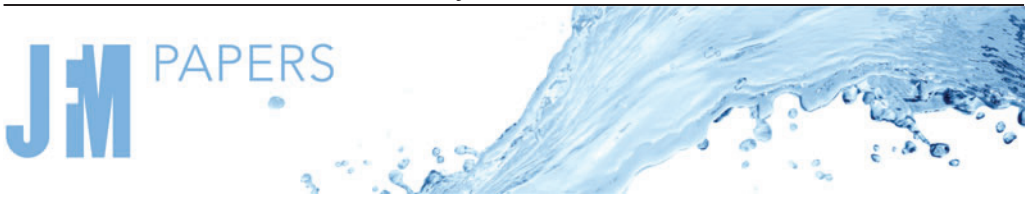

Vortex dynamics in rotating Rayleigh–Bénard convection

Shan-Shan Ding[1], Guang-Yu Ding[2,3], Kai Leong Chong[3,4], Wen-Tao Wu[1], Ke-Qing Xia[2,3,†] and Jin-Qiang Zhong[1,5,†]

[1]School of Physics Science and Engineering, Tongji University, Shanghai 200092, PR China

[2]Center for Complex Flows and Soft Matter Research and Department of Mechanics and Aerospace Engineering, Southern University of Science and Technology, Shenzhen 518055, PR China

[3]Department of Physics, The Chinese University of Hong Kong, Shatin, Hong Kong, PR China

[4]Shanghai Institute of Applied Mathematics and Mechanics, School of Mechanics and Engineering Science, Shanghai University, Shanghai 200072, PR China

[5]Department of Aeronautics and Astronautics, Fudan University, Shanghai 200433, PR China

(Received 22 May 2023; revised 8 September 2023; accepted 2 October 2023)

We investigate the spatial distribution and dynamics of the vortices in rotating Rayleigh–Bénard convection in a reduced Rayleigh number range $1.3 \leq Ra/Ra_c \leq 83.1$. Under slow rotations ($Ra \approx 80\,Ra_c$), the vortices are distributed randomly, which is manifested by the size distribution of the Voronoi cells of the vortex centres being a standard Γ distribution. The vortices exhibit Brownian-type horizontal motion in the parameter range $Ra \gtrsim 10\,Ra_c$. The probability density functions of the vortex displacements are, however, non-Gaussian at short time scales. At modest rotating rates ($4\,Ra_c \leq Ra \lesssim 10\,Ra_c$), the centrifugal force leads to radial vortex motions, i.e. warm cyclones (cold anticyclones) moving towards (outwards from) the rotation axis. The horizontal scale of the vortices decreases with decreasing Ra/Ra_c, and the size distribution of their Voronoi cells deviates from the Γ distribution. In the rapidly rotating regime ($1.6\,Ra_c \leq Ra \leq 4\,Ra_c$), the vortices are densely distributed. The hydrodynamic interaction of neighbouring vortices results in the formation of vortex clusters. Within clusters, cyclones exhibit inverse-centrifugal motion as they submit to the outward motion of the strong anticyclones, and the radial velocity of the anticyclones is enhanced. The radial mobility of isolated vortices, scaled by their vorticity strength, is shown to be a simple power function of the Froude number. For all flow regimes studied, we show that the number of vortices with a lifespan greater than t decreases exponentially as $\exp(-t/\tau)$ for large time, where τ represents the characteristic lifetime of long-lived vortices.

Key words: Bénard convection, turbulent convection, rotating flows

† Email addresses for correspondence: xiakq@sustech.edu.cn, jinqiang@fudan.edu.cn

1. Introduction

Buoyancy-driven convection is relevant to many natural flows in the atmosphere, oceans and planetary systems (Marshall & Scott 1999; Vallis 2006; Jones 2011). A rich variety of vortex structures arises during buoyant convection, especially in the presence of background rotations (Hopfinger & van Heijst 1993). Vortices are often referred to as coherent structures that consist of recirculating flows with roughly circular streamlines. The dynamics of vortices plays an important role in determining fluid motions and turbulent transport, ranging from small-scale turbulence to planetary-scale circulations (Fernando & Smith 2001). The dynamics of convective vortices can be studied using a paradigmatic model, rotating Rayleigh–Bénard convection (RBC), i.e. a fluid layer heated from below and rotated about a vertical axis. In rotating RBC, the fluid flows are governed by a set of non-dimensional parameters including the Rayleigh number (Ra) describing the strength of thermal forcing, the Ekman number (Ek) representing the rotating effect, the Froude number (Fr) for the strength of the centrifugal force, the Prandtl number (Pr) for the fluid properties, and the aspect ratio Γ_a describing the geometry of the fluid domain:

$$Ra = \frac{g\alpha\,\Delta T\,H^3}{\kappa\nu}, \quad Ek = \frac{\nu}{2\Omega^2 H}, \quad Fr = \frac{\Omega^2 D_0}{2g}, \quad Pr = \frac{\nu}{\kappa}, \quad \Gamma_a = D_0/H. \quad (1.1a\text{–}e)$$

Here, g denotes the gravity acceleration, ΔT is the applied temperature difference, D_0 and H are the horizontal and vertical length scales of the fluid domain, respectively, and α, κ and ν are the thermal expansion, thermal diffusivity and kinematic viscosity of the working fluid. Ω is the applied rotating velocity along a vertical axis.

A number of previous investigations report that for rapidly rotating RBC, the convective flows are organized by the Coriolis force into columnar vortices (Boubnov & Golitsyn 1986; Sakai 1997; Vorobieff & Ecke 2002; Portegies *et al.* 2008; King *et al.* 2009; Grooms *et al.* 2010; Kunnen, Clercx & Geurts 2010; Julien *et al.* 2012; Shi *et al.* 2020). The structure of a columnar vortex can be described by the theory of thermal wind balance, which states that vertical velocity gradients are caused by horizontal temperature gradients in the flow field (Kundu & Cohen 2008):

$$2\Omega\,\frac{\partial \boldsymbol{u}}{\partial z} = -\alpha g\,\widehat{\boldsymbol{e}_z} \times \boldsymbol{\nabla} T. \quad (1.2)$$

When observed in the lower fluid level, upwelling warm fluid elements rotate in the same direction as the system when they experience horizontal advection, forming cyclones. Oppositely, cold downwelling fluid elements are organized into anticyclones. Under thermal wind balance, the horizontal gradient in the right-hand side of (1.1*a–e*) alters the vertical velocity and vorticity in magnitude along the vertical axis, and their signs around the middle plane. Both types of vortices are tall, thin, coherent convection columns with their horizontal scale given by $l = (2\pi^4)^{1/6}\,Ek^{1/3}\,H$ for high-Pr fluids in the limit of rapid rotations (Chandrasekhar 1961; Julien & Knobloch 1998; Aurnou, Bertin & Grannan 2018). The number density n of the columnar vortices increases when Ek decreases. It is found in previous studies that n can be described by a power function of Ek, i.e. $n \propto Ek^{\alpha_n}$ (Boubnov & Golitsyn 1986; Sakai 1997; Vorobieff & Ecke 2002; Kunnen *et al.* 2010). Different scaling exponents α_n varying from -1.5 to -0.4 are reported in these studies, which is presumably ascribed to the different fluid heights where measurements are made

and the various criteria are used to identify vortices. The mean spacing between the columnar vortices is given by $d_v \propto \sqrt{1/n}$ (Sakai 1997), assuming that the vortices are distributed uniformly. However, when the spatial distribution of the vortices is not uniform, as observed by Chong *et al.* (2020) and Ding *et al.* (2021) in rapidly rotating RBC, the vortex spacing d_v is not simply a square-root function of n, thus a more comprehensive description of the vortex spatial distribution is required.

The flow structure of the columnar vortices in rotating RBC was investigated in numerical simulation (Julien *et al.* 1996) and in laboratory experiments (Vorobieff & Ecke 1998). These studies discovered that each columnar vortex is surrounded by a shielding layer. The signs of vorticity, temperature anomaly and vertical velocity in the shield layer are opposite to those in the vortex core region. Portegies *et al.* (2008) proposed a theoretical model for the flow structures of the columnar vortices, in which they consider linearized governing equations of fluid motion and provide analytical solutions for the radial profiles of temperature fluctuations, vertical velocity and vorticity. An asymptotic theory of rapidly rotating RBC was developed by Sprague *et al.* (2006) and Grooms *et al.* (2010), where they suggested that in the limit of extremely rapid rotations, the columnar vortex structure is steady and axially and vertically symmetric, and predicted that the poloidal stream function of the vortices can be described by the zero-order Bessel function of the first kind (Grooms *et al.* 2010). It follows that both the radial profiles of the azimuthal velocity and the vertical vorticity can be expressed by prescribed Bessel functions. These predictions appeared to match with numerical simulations (Grooms *et al.* 2010; Nieves, Rubio & Julien 2014). Recently, Shi *et al.* (2020) performed spatially resolved measurements of the fine structures of the columnar vortices. Their results reveal that the asymptotic theory predicts accurately the velocity and vorticity profiles of the vortices in the flow regime of rotation-dominated convection, but deviates from the experimental results in weakly rotating convection. The three-dimensional experimental vorticity structure of vortices was measured by Fujita *et al.* (2020) through scanning velocity fields at different heights.

Numerical simulations in the full parameter space of rotating convection have revealed distinct flow structures with increasing buoyancy forcing, namely, cellular convection (Cell), convective Taylor columns (Columns), plumes and geostrophic turbulence (Julien *et al.* 2012; Nieves *et al.* 2014; Stellmach *et al.* 2014). It is shown that in the flow regime of Columns, the shield structure of the columnar vortices weakens with increasing *Ra* and finally disappears. The violent vortex interactions then destroy the coherent columns and lead to the formation of plume-like structures (Stellmach *et al.* 2014). Rajaei, Kunnen & Clercx (2017) performed measurements of the spatial vorticity autocorrelations to reveal the periodicity of the flow structures. Their experimental results indicated a sharp change in the slope of the correlation function, indicating a transition from the cellular–columnar state to the plume state. Shi *et al.* (2020) measured the vorticity gradient at the shielding layer to determine quantitatively the strength of the vortex shield structures. They showed that the mean vorticity gradient followed two distinct scaling relations with increasing *Ra*, and suggested a flow state transition from weakly rotating convection to rotation-dominated, geostrophic convection.

Along with the large number of studies devoted to exploring the flow structures and spatial distribution of the vortices in rotating RBC, some efforts have been made to inspect the dynamics of these vortices. Early experiment observations suggest that these convective vortices exhibit diverse dynamical states of horizontal motion, ranging from quasi-stationary, vortex merging to intensive advection (Boubnov & Golitsyn 1986; Zhong, Ecke & Steinberg 1993; Sakai 1997; Vorobieff & Ecke 2002; King & Aurnou 2012). Chong *et al.* (2020) demonstrate through both experiment and numerical

simulation that the vortices undergo horizontally diffusive motion and resemble that of inertial Brownian particles, i.e. they move ballistically in a short time but then diffusively in a large time scale. They reported that the diffusion motion of the vortices is in the type of pure Brownian motion, since the vortex velocity autocorrelation function decays exponentially in time, and the transition from ballistic to diffusive motion is sharp. Under rapid rotations, the centrifugal force plays a role in influencing the vortex motion. Noto *et al.* (2019) observed the radial acceleration of the vortices in rotating RBC. Hu *et al.* (2021) used a convection cell placed at a distance away from the rotation axis in which they can vary the Froude number with a fixed Ekman number to study the centrifugal effects. They reported an onset of flow bifurcation above which the relatively cold and warm vortices moved in opposite directions, with cold (warm) vortices concentrated in the far (near) region. Ding *et al.* (2021) proposed an extended Langevin equation incorporating centrifugal (centripetal) force to interpret the radial motion of cold (warm) vortices:

$$\ddot{r} + \dot{r}/t_c \mp \zeta r = \xi(t), \tag{1.3}$$

where r represents the radial position of the vortex centre, t_c is the relaxation time scale, ζ is the centrifugal coefficient, and ξ denotes the stochastic term correlated in time in the form of the delta function, i.e. white noise. The analytical solution of this model gives the first moment of radial displacement at a large time scale as an exponential function,

$$\langle r/r_0 \rangle_\xi \propto \exp(\pm\lambda^* t), \tag{1.4}$$

where the radial mobility $\lambda^* \approx |1/(2t_c) - \sqrt{1/(4t_c^2) \pm \zeta}|$ represents the fastest growth (or slowest decay) rate for anticyclones (cyclones). The plus and minus signs in (1.4) represent solutions for cold and warm vortices, respectively. This model sheds light on the 'super-diffusive' behaviour of vortex motion (Noto *et al.* 2019; Ding *et al.* 2021), which is a result of the directional radial motion. Ding *et al.* (2021) also reported in the centrifugation-dominated flow regime the counterintuitive effect of hot vortices moving outwards from the rotation axis collectively, which is interpreted as a result of long-range vortex interactions. Recently, Ding *et al.* (2022) reported that when periodic topographic structures are constructed on the heated boundary in rotating RBC, the stochastic translational motion of the columnar vortices can be strictly controlled to form stationary convection patterns with prescribed symmetries.

Despite previous studies of vortex motion in rotating RBC, a definitive relationship between the radial velocity of the vortices and its driven force, i.e. the centrifugal buoyancy, has yet to be established. The challenge in establishing their relationship arises from the complication caused by the formation of vortex clusters (Ding *et al.* 2021). In such a fluid system with its flow field characterized by horizontally meandering vortices, an important question arises concerning the connection between vortex distribution and their horizontal motion. Additionally, in the context of translational vortex motion, the lifespan of the vortices is an essential aspect that accounts for the stable spatial distribution of the vortex number density as observed in experiments. The long-lived convective vortices are shown to play a crucial role in the transport of heat and material across large-scale regions (Gascard *et al.* 2002). However, the statistical properties of the lifespan of vortices in rotating RBC remain unexplored.

We present in this paper an extensive investigation of the vortex distribution, lifespan and dynamics in rotating RBC across a wide range of control parameters (see experimental details in § 2). Discussions of the vortex spatial distribution are presented in § 3, followed by the vortex displacement distribution in § 4. The regimes of vortex dynamics are given

in § 5. A simple relation between vortex radial motion and Froude number is derived in § 6. The lifespan of vortices is discussed in § 7. A summary and discussion of the results are provided in § 8.

2. Experimental and numerical methods

2.1. *Experimental set-up and parameters*

The experimental apparatus was designed for high-resolution flow field measurements in rotating RBC (Chong *et al.* 2020; Shi *et al.* 2020; Ding *et al.* 2021). Here, we present only its essential features. The bottom plate of the convection cell was made of oxygen-free, high-conductivity copper. Its bottom side was covered uniformly by parallel straight grooves. A main heater made of resistance wires was epoxied into the grooves. Seven thermistors were installed into the bottom plate, at vertical distance 3.5 mm from the top surface of the plate. The main heater was operated in a digital feedback loop in conjunction with these thermistors to hold the bottom-plate temperature as a constant with a stability of a few millikelvins. For the purpose of flow visualization, we used a top plate made of a 5 mm thick sapphire disc. A thermal bath that contained circulating coolant was constructed over the sapphire plate and regulated its temperature. During the experiment, the temperature fluctuation of the top plate was within 0.005 K.

The temperature difference between the bottom plate and the ambient air may induce thermal perturbations to the experiment. To eliminate this temperature difference, a bottom adiabatic shield was installed under the bottom plate. This thermal shield was covered by a bottom-shield heater, with a thermistor located at the centre of the shield. A second auxiliary heater was wound around the periphery of the shield, and the local temperature there was measured by a second thermistor. Both heaters worked in conjunction with their relevant thermistors to maintain the bottom-shield temperature the same as the bottom-plate temperature.

In between the top and bottom plates was a cylindrical sidewall made of plexiglas with a thickness of 3 mm. Thermal protection towards the sidewall was provided by a separate thermal side shield. It was a thin cylindrical ring made of aluminium, with a spiral aluminium tube wound on its outer surface. A circulating flow of coolant passed through the aluminium tube kept the side-shield temperature at the mean fluid temperature. Most of the spatial volume in between the thermal shields and the convection cell was filled with low-density open-pore foam to prevent convective air flows. The aforementioned two coolant circuits were brought into the rotary table through a rotary union. It was a four-passage feed through equipped with a slip ring for electrical leads. The rotary table rotated clockwise driven by an electric servo-motor. All components of the convection cell were installed on the rotary table.

In the present study, we used two cylindrical cells with an inner diameter $D_0 = 240$ mm, and fluid height $H = 63.0$ (120.0) mm, yielding the aspect ratio $\Gamma_a = D_0/H = 3.8$ (2.0). Deionized water was the working fluid, with a constant Prandtl number $Pr = \nu/\kappa = 4.38$. The experiment was conducted in the range $2.0 \times 10^7 \leq Ra \leq 2.7 \times 10^8$ of the Rayleigh number $Ra = \alpha g\, \Delta T\, H^3/\kappa\nu$ (where α is the isobaric thermal expansion coefficient, g is the acceleration of gravity, ΔT is the applied temperature difference, κ is the thermal diffusivity, and ν is the kinematic viscosity). For each dataset with the same Ra, all measurements were made at constant ΔT, with Ω varying from 0.31 to 5.0 rad s^{-1}. The Ekman number $Ek = \nu/(2\Omega H^2)$ spanned $1.7 \times 10^{-5} \leq Ek \leq 2.7 \times 10^{-4}$. The Froude number $Fr = \Omega^2 D_0/2g$ was within $1.2 \times 10^{-3} \leq Fr \leq 0.31$. The convection in the

Group	$10^{-7}Ra$	Γ	Regime	10^5Ek	Ra/Ra_c	Fr
EXP1	2.0	3.8	Cell	1.79, 1.92, 2.24	1.30, 1.43, 1.76	0.272, 0.237, 0.174
			Columns	2.68	2.26	0.121
			Plumes	3.36, 4.47, 5.37	3.07, 4.57, 5.87	0.077, 0.044, 0.030
			BD	13.4, 26.8	20.9, 54.8	0.005, 0.001
EXP2	3.0	3.8	Cell	1.68, 1.79	1.80, 1.97	0.309, 0.272
			Columns	1.92, 2.24	2.16, 2.67	0.237, 0.174
			Plumes	2.68, 3.36, 4.47, 5.37	3.43, 4.66, 6.93, 8.90	0.121, 0.077, 0.044, 0.030
			BD	8.95, 13.4, 26.8	18.0, 31.6, 83.1	0.011, 0.005, 0.001
EXP3	14	2.0	Cell	0.493	1.54	0.272
			Columns	0.617, 0.740	2.09, 2.68	0.174, 0.121
			Plumes	0.925, 1.23, 1.48	3.64, 5.39, 6.91	0.077, 0.044, 0.030
EXP4	27	2.0	Columns	0.493	3.09	0.272
			Plumes	0.617, 0.740, 0.925, 1.23	4.18, 5.36, 7.27, 10.8	0.174, 0.121, 0.077, 0.044
DNS	2.0	4.0	Cell	1.78, 1.90, 2.22	1.30, 1.42, 1.76	0.270, 0.240, 0.174
			Columns	2.66	2.26	0.120
			Plumes	3.33, 3.67, 4.44, 5.41, 7.00, 9.18	3.07, 3.51, 4.57, 5.99, 8.55, 12.4	0.077, 0.064, 0.040, 0.029, 0.017, 0.010
			BD	12.1, 18.2, 26.6	18.3, 32.2, 54.7	0.006, 0.003, 0.001

Table 1. Parameters of all experimental runs. Results for $\Gamma = 3.8, 2.0$ are acquired from convection cells with $H = 63, 120$ mm, respectively. The dynamical regimes are determined based on Julien *et al.* (2012), Kunnen (2021) and Lu *et al.* (2021). BD is an abbreviation for the buoyancy-dominated regime.

experiment is assured by examining the reduced number Ra/Ra_c greater than 1, where $Ra_c = (8.7 - 9.63\,Ek^{1/6})\,Ek^{-4/3}$ (Niiler & Bisshopp 1965) is the critical value for the onset of convection in a horizontally infinitely large system. More information about various parameter regimes is reported in table 1.

We conducted measurements of the horizontal velocity field (u_x, u_y) using a particle image velocimetry system installed on the rotary table. A thin light sheet powered by a solid-state laser illuminated the seed particles in a horizontal plane at fluid height $z = H/4$. Images of the particle were captured through the top sapphire window by a high-resolution camera (2456 × 2058 pixels). Two-dimensional velocity fields were extracted by cross-correlating two consecutive particle images. Each velocity vector was calculated from an interrogation window (32 × 32 pixels), with 50 % overlap of neighbouring sub-windows to ensure sufficient resolution of the velocity field (Westerweel, Elsinga & Adrian 2013; Shi *et al.* 2020). Thus we obtained 154 × 129 velocity vectors on each frame, reaching resolution 2.0 mm for the velocity field. We identify the vortices through a two-dimensional Q-criterion. Considering the quantity $Q = (\mathrm{Tr}\,\boldsymbol{A})^2 - 4\det\boldsymbol{A}$ with the velocity gradient tensor $\boldsymbol{A} = [\partial(u_x, u_y)/\partial(x, y)]$, we define the vortex centre as the minimum of Q within a vortex region satisfying $Q < -Q_{std}$. Here, Q_{std} is the standard deviation of Q over the measured area $r \leq D_0/4$ (Chong *et al.* 2020; Ding *et al.* 2021). We adopt the method of vortex tracking introduced in Ding *et al.* (2021) to obtain vortex trajectories.

2.2. Numerical method

In the direct numerical simulations (DNS), we solved the three-dimensional Navier–Stokes equations within the Boussinesq approximation:

$$\frac{\mathrm{D}\boldsymbol{u}}{\mathrm{D}t} = -\boldsymbol{\nabla} P + \left(\frac{Pr}{Ra}\right)^{1/2} \nabla^2 \boldsymbol{u} + \theta \hat{z} + \left(\frac{Pr}{Ra\,Ek^2}\right)^{1/2} \boldsymbol{u} \times \hat{z} - \frac{2r\,Fr}{D}\,\theta \hat{r}, \tag{2.1}$$

$$\frac{\mathrm{D}\theta}{\mathrm{D}t} = \frac{1}{(Ra\,Pr)^{1/2}} \nabla^2 \theta, \tag{2.2}$$

$$\boldsymbol{\nabla} \cdot \boldsymbol{u} = 0. \tag{2.3}$$

Here, $\boldsymbol{u}$ is the fluid velocity, and θ and P are the reduced temperature and pressure.

Equations (2.1)–(2.3) were non-dimensionalized using H, ΔT and the free-fall velocity $U_f = \sqrt{\alpha g\,\Delta T H}$. The top (bottom) plate was isothermal with temperature $\theta_t = -0.5$ ($\theta_b = 0.5$), and the sidewall was thermally insulated. As for the momentum boundary condition, all boundaries were no-slip. These equations were solved using the multiple-resolution version of *CUPS* (Kaczorowski & Xia 2013; Chong, Ding & Xia 2018), which was a fully parallelized DNS code based on a finite-volume method with fourth-order precision. To improve computational efficiency without any sacrifice in precision, we used a multiple-resolution strategy. The grid resolutions along the radial, azimuthal and vertical directions were $140 \times 384 \times 160$ for the momentum and pressure fields, and $280 \times 768 \times 160$ for the temperature field. We examine the ratios between the vertical grid spacing and the local Kolmogorov and Batchelor length scales. The maximum value of these two ratios for all cases is about 1.2, and for most of the cases, these two ratios are well below unity. Additionally, the thickness of the Ekman boundary layer decreases as Ek decreases. We ensured that there were no fewer than 11 grid points within the Ekman layer even for the smallest Ek of the present work, to resolve the Ekman boundary layer sufficiently. The simulations were performed in a cylindrical domain with $\Gamma_a = 4$, $Ra = 2.0 \times 10^7$, $Pr = \nu/\kappa = 4.38$ and $1.3 \leq Ra/Ra_c \leq 55$.

3. Vortex spatial distribution

In the rotating RBC, the spatial distribution and organization of the convective vortices depend sensitively on the strength of rotation and buoyancy. To demonstrate the distribution of the columnar vortices, we present in figure 1 Voronoi diagrams of the vortex centres for two reduced Rayleigh numbers, $Ra/Ra_c = 8.90$ and 2.67. The background colour of these diagrams represents the distribution of the Q field, where vortices are shown in reddish colour, and the bluish areas in between indicate regions of high flow strain. We see that under weak rotations, the vortices appear to be located randomly with a broad size distribution for $Ra/Ra_c = 8.90$. The Voronoi cells become smaller on average but seemingly have an even size distribution for rapid rotations ($Ra/Ra_c = 2.67$).

In the following analysis, we consider the probability density functions (PDFs) of Voronoi cell area of the vortices. It has been shown that for randomly distributed entities in d-dimensional space ($d \leq 3$), the PDF of their Voronoi areas (volumes) normalized by the mean is the standard Γ distribution (Ferenc & Néda 2007; Tagawa *et al.* 2012):

$$P(x) = \frac{[(3d+1)/2]^{(3d+1)/2}}{\Gamma[(3d+1)/2]}\, x^{(3d-1)/2} \exp(-[(3d+1)/2]x). \tag{3.1}$$

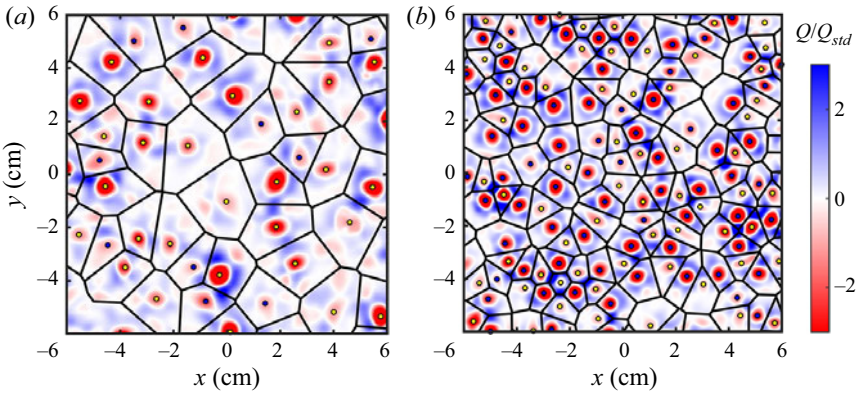

Figure 1. Spatial distribution of the vortices for (*a*) weakly rotating convection and (*b*) rotation-dominated convection. The solid line network constitutes the Voronoi diagram of the vortex centres. The background colouration represents the distribution of the quantity Q/Q_{std}, with blue (yellow) dots denoting the centres of anticyclones (cyclones). Experimental results for $Ra = 3.0 \times 10^7$ and for (*a*) $Ra/Ra_c = 8.90$ and (*b*) $Ra/Ra_c = 2.67$.

Here, the denominator is a Γ function. For two-dimensional distributions ($d = 2$), we have $P_2(x) = 7^{7/2}2^{-7/2}x^{5/2}\exp(-7x/2)/\Gamma(7/2)$. The Voronoi diagram offers a qualitative scheme to describe the spatial distributions of entities in densely populated systems (Ferenc & Néda 2007; Tagawa *et al.* 2012). For example, the clustering effect of particles in turbulence leads to an increase of the standard deviation of the scaled Voronoi volumes of the particles, and thus the PDF of the Voronoi volumes deviates from the standard Γ distribution (Tagawa *et al.* 2012).

Figure 2(*a*) shows the PDFs of the Voronoi cell areas A of the vortices normalized by the mean value $P(A/\langle A\rangle)$. We see that for $Ra/Ra_c = 83.09$, $P(A/\langle A\rangle)$ follows closely the standard Γ distribution $P_2(x)$. With increasing rotation rates (decreasing Ra/Ra_c), the PDFs of the Voronoi cell area show behaviour different from that of the standard Γ distribution. We see that the PDFs have a smaller possibility for very large and small cells than for random distributed ones, but a larger probability for $A/\langle A\rangle \approx 1$. These results suggest that the vortices are indeed randomly distributed for a sufficiently large Ra/Ra_c. The size distribution of the Voronoi cells of the vortices becomes relatively uniform when Ra/Ra_c decreases.

Figures 2(*b*) and 2(*c*) present the mean value $\langle A\rangle$ and the standard deviation $\sigma(A/\langle A\rangle)$ of the Voronoi cell area as functions of Ra/Ra_c. Our experimental and numerical data show that $\langle A\rangle$ decreases monotonically with decreasing Ra/Ra_c, signifying an increasing vortex number density. The standard deviation $\sigma(A/\langle A\rangle)$, however, exhibits the interesting trend that for $Ra/Ra_c = 83.09$, it reaches approximately the value of a standard Γ distribution, $\sigma_0 = \sqrt{(3d+1)/2} = \sqrt{2/7}$. With decreasing Ra/Ra_c, $\sigma(A/\langle A\rangle)$ decreases and reaches a minimum value at $Ra/Ra_c \approx 4$. When $Ra/Ra_c \leq 4$, $\sigma(A/\langle A\rangle)$ starts to increase. The emergence of the minimum of $\sigma(A/\langle A\rangle)$ at $Ra/Ra_c \approx 4$ can be seen also in figure 2(*a*). The decreasing of $\sigma(A/\langle A\rangle)$ for $Ra/Ra_c \geq 4$ implies the homogenized size distribution of the Voronoi cells with decreasing Ra/Ra_c in the weakly rotating regime where the vortices are sparsely distributed. For $Ra/Ra_c \leq 4$, however, the increase of $\sigma(A/\langle A\rangle)$ may be ascribed to the formation of large-scale vortex clusters, as we will discuss in § 6.

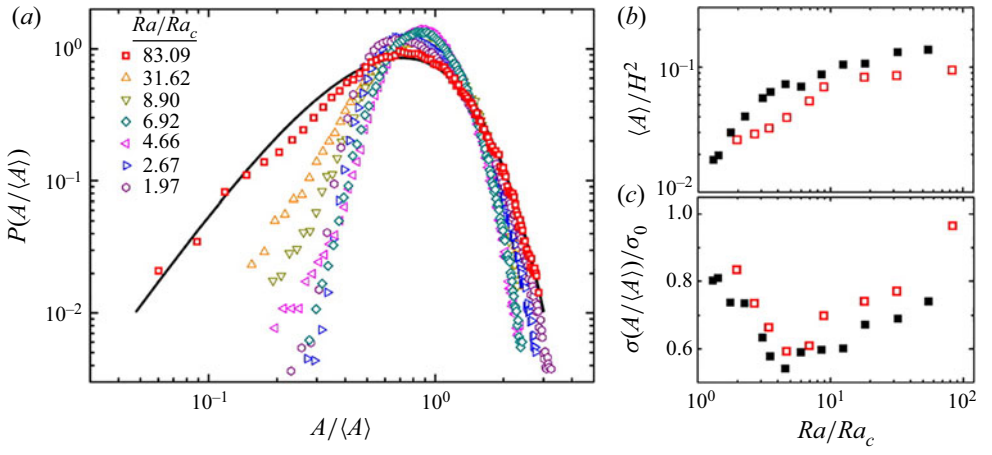

Figure 2. (*a*) The PDFs of the Voronoi cell area $P(A/\langle A\rangle)$ for various Ra/Ra_c. The solid curve represents the two-dimensional Γ distribution $P_2(A/\langle A\rangle)$. (*b*) The normalized mean area $\langle A\rangle/H^2$ of the Voronoi cells as a function of Ra/Ra_c. (*c*) The rescaled standard deviation $\sigma(A/\langle A\rangle)/\sigma_0$ as a function of Ra/Ra_c, with $\sigma_0 = \sqrt{2/(3d+1)} = \sqrt{2/7}$. Open symbols: experimental data for $Ra = 3.0 \times 10^7$. Closed symbols: numerical data for $Ra = 2.0 \times 10^7$.

4. Probability density distribution of vortex displacements

Through tracking the horizontal motion of the vortices, we obtain their trajectories $\boldsymbol{r}(t)$ and calculate the mean square displacement (MSD) for the vortices for a given time interval t, i.e. $\langle \delta r^2\rangle(t) = \langle(\boldsymbol{r}(t+t_0) - \boldsymbol{r}(t_0))^2\rangle_{t_0}$, where $\langle\,\cdot\,\rangle_{t_0}$ denotes the average over all time stamps t_0 and all vortex trajectories. Figure 3(*a*) shows results of $\langle \delta r^2\rangle/t$ as a function of t for various Ra/Ra_c. We see that in the weakly rotating regime with $Ra/Ra_c \geq 8.9$, $\langle \delta r^2\rangle/t$ can be well described as

$$\langle \delta r^2\rangle/t = 2D[1 - t_c/t(1 - \exp(-t/t_c))], \tag{4.1}$$

which implies that the vortex motion is Brownian-type, random motion. Here, t_c represents the transitional time from the ballistic to the diffusive regime, and D is the diffusivity (Chong *et al.* 2020).

To gain deep insight into the stochastic properties of the vortex motion under weak rotations, we study the PDFs of the vortex displacement $P(\mathrm{d}x, \mathrm{d}t)$ in one dimension $\mathrm{d}x$ for different time intervals $\mathrm{d}t$. Figures 3(*b*) and 3(*d*) show experimental and numerical data for $Ra/Ra_c = 18.0$, respectively. We see that for a large time interval $\mathrm{d}t \geq t_c$, $P(\mathrm{d}x)$ is Gaussian to good precision, as one would expect for normal Brownian motion. For a very small time interval $\mathrm{d}t \leq t_c$, however, $P(\mathrm{d}x)$ appears to deviate from a Gaussian function. In order to estimate the deviation of $P(\mathrm{d}x)$ from a Gaussian distribution with decreasing $\mathrm{d}t$, we calculate the excess kurtosis α, which characterizes the departure from Gaussianity, $\alpha = \langle(\mathrm{d}x - \langle \mathrm{d}x\rangle)^4\rangle/[3\langle(\mathrm{d}x - \langle \mathrm{d}x\rangle)^2\rangle^2] - 1$. Thus $\alpha = 0$ indicates a perfect Gaussian distribution, and a large α signifies a departure from Gaussian. Figure 3(*c*) shows the results of α as a function of $\mathrm{d}t/t_c$ for four sets of Ra/Ra_c. One sees that $\alpha \leq 0.1$ for large time interval $\mathrm{d}t \geq t_c$. However, when $\mathrm{d}t$ decreases below t_c, α increases rapidly and becomes significant for very small $\mathrm{d}t$. Results of MSDs and PDFs of the vortex displacement (figure 3) suggest that on very short time scales, the vortex undergoes non-Gaussian yet ballistic motion. A full theoretical interpretation of such dynamical properties of vortices remains to be studied.

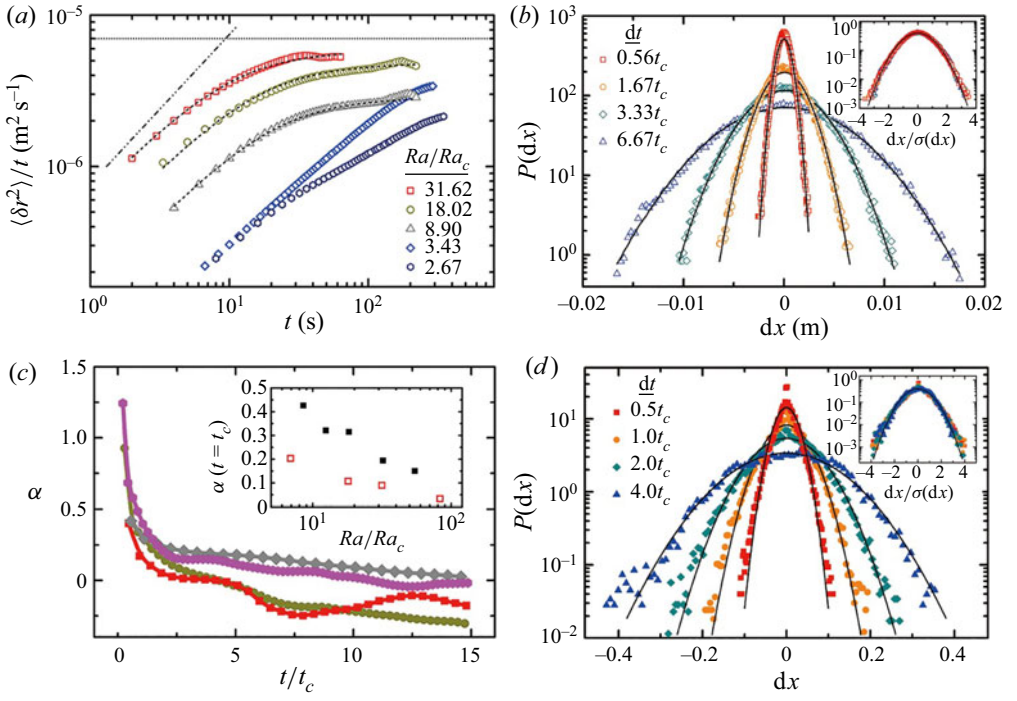

Figure 3. (*a*) Results for $\langle \delta r^2 \rangle / t$ as a function of t for various Ra/Ra_c. The dashed lines present the theoretical fits to the data for weakly rotating convection based on (4.1). The dash-dotted line indicates a scaling $\langle \delta r^2 \rangle \sim t^2$ in the ballistic regime. Results for $Ra = 3.0 \times 10^7$. (*b*,*d*) The PDFs of the vortex displacement $P(\mathrm{d}x)$ at various time intervals $\mathrm{d}t$. Experimental (*b*) and numerical (*d*) data for $Ra/Ra_c = 18.0$. Insets in (*b*,*d*) show the rescaled PDFs $P(\mathrm{d}x/\sigma(\mathrm{d}x))$ where the vortex displacement $\mathrm{d}x$ is normalized by its standard deviation $\sigma(\mathrm{d}x)$. (*c*) The non-Gaussian parameter α as a function of t/t_c. Numerical results for $Ra/Ra_c = 54.0$ (red squares), 18.25 (green circles), 12.45 (grey diamonds) and 8.55 (purple hexagons). Inset in (*c*) shows α as a function of Ra/Ra_c for $t = t_c$. Open symbols: experimental data for $Ra = 3.0 \times 10^7$. Closed symbols: numerical data for $Ra = 2.0 \times 10^7$.

Here, we infer that in a small time scale, the random motion of the vortices, driven by the turbulent fluctuations of the background flows, is largely disturbed by the passing vortices. The vortex interactions, such as merging (annihilation) of same (opposite) sign neighbouring vortices, result in intermittent but deterministic horizontal movements of the vortices in a short time. The observed PDFs of the vortex displacement in this time scale are thus non-Gaussian. As the time interval $\mathrm{d}t$ increases and so does the vortex displacement $\mathrm{d}x$, the intermittent perturbation from a single adjacent vortex gives way to the complex interactions from multiple neighbouring vortices that appear to have stochastic spatiotemporal properties. In addition, owing to the large-amplitude background turbulent fluctuations that dominate the vortex motion in large time scales, the PDF of the vortex displacements returns to Gaussianity. We investigate the non-Gaussian parameter α as a function of Ra/Ra_c for a given time interval $\mathrm{d}t = t_c$ in the inset plot of figure 3(*c*). Our experimental and numerical data suggest that in this weakly rotating regime, α increases when Ra/Ra_c decreases. A similar trend of increasing α with decreasing Ra/Ra_c is found when other time intervals $\mathrm{d}t$ are chosen. With decreasing Ra/Ra_c, the diffusivity of a vortex becomes weaker (Chong *et al.* 2020), and the mean travelling distance of the vortices decreases. Then each vortex comes across fewer vortices. As a

result, the interaction between adjacent vortices becomes more intermittent. Moreover, the magnitude of the background turbulent fluctuations decreases with decreasing Ra/Ra_c. Its impact on the random motion of vortices becomes less significant than that of the intermittent vortex interaction. For these reasons, we see that the stochastic motion of vortices becomes more non-Gaussian, as reflected by the increase of α.

5. Regimes of vortex motion

Figure 3(*a*) shows that with the increasing rotating rate ($Ra/Ra_c \leq 4$), the MSD of the vortices increases faster than a linear function at large times. Such behaviour of the vortices is ascribed to the centrifugal force that gives rise to the radial vortex motion. Based on our Langevin model incorporating the centrifugal force (introduced in § 1), the radial velocity of vortices is expected to be proportional to their radial position,

$$\langle u_r \rangle_\xi = \lambda^* r. \tag{5.1}$$

Here, $\lambda^* = |1/(2t_c) - \sqrt{1/(4t_c^2) \pm \zeta}|$ is the radial mobility for anticyclones and cyclones, respectively, and $\langle \cdot \rangle_\xi$ denotes the ensemble average over the vortex trajectories (Ding *et al.* 2021).

Figure 4 shows, as functions of the radial position, the mean values of the radial velocity $\langle u_r \rangle_\xi$, number density $\langle n \rangle_\xi$ and vorticity magnitude $\langle |\omega| \rangle_\xi$ of both types of vortices. Four distinct flow regimes are identified clearly. We first find in a weakly rotating regime ($Ra/Ra_c = 54.8$ and $Fr = 0.030$) that $\langle u_r \rangle_\xi$ for both types of vortices fluctuates around zero, indicating the absence of radial motion (figure 4*a*). In this flow regime, we note that the mean values of number density $\langle n \rangle_\xi$ and vorticity magnitude $\langle |\omega| \rangle_\xi$ for cyclones are significantly greater than those for anticyclones (figures 4*e*,*i*). This is the case because anticyclones are downwelling vortices generated from the top boundary. When observed at the lower half of the fluid layer, they travel a longer distance to the measured fluid height ($z = H/4$) than the upwelling vortices (cyclones), and their momentum and vorticity have been largely dissipated by the background turbulence. (Values of $\langle n \rangle_\xi$ and $\langle |\omega| \rangle_\xi$ for the two types of vortices would be equal if measured at $z = H/2$; see discussions in Ding *et al.* 2021.) In the sidewall region ($r/R > 0.85$), large fluctuations of all the measured variables appear owing to the intensive perturbation of the flow field by the boundary zonal flows (de Wit *et al.* 2020; Zhang *et al.* 2020).

When the rotating rate increases ($Ra/Ra_c = 4.57$, $Fr = 0.044$), we see that $\langle u_r \rangle_\xi$ of anticyclones (cyclones) is larger (smaller) than zero, indicating that anticyclones (cyclones) move away from (towards) the rotation axis under the centrifugal force. Figure 4(*b*) shows that $\langle u_r \rangle_\xi$ increases (or decreases) linearly with r for anticyclones (cyclones), which is well predicted by (5.1). Cyclonic vortices still possess a greater number density and vorticity magnitude than those of anticyclones at the measurement height (figures 4*f*,*j*). With further increase of Ω, the centrifugal effect becomes dominant. For $Ra/Ra_c = 2.26$, $Fr = 0.12$, we note that unexpectedly, $\langle u_r \rangle_\xi$ for both vortices is positive and increases linearly with r in the inner region (figure 4*c*), signifying that cyclones exhibit outward motion that is opposite to the centrifugal effect. For both types of vortices, $\langle u_r \rangle_\xi$ reaches a maximum at a radial position that depends on Ra/Ra_c, and then decreases with larger r in the outer region. In the central region, we find that both the number density and vorticity magnitude of anticyclones exceed those of the cyclones (figures 4*g*,*k*). In the limit of rapid rotation with $Ra/Ra_c = 1.43$, $Fr = 0.24$, the cyclones are found to take up the inward radial motion with $\langle u_r \rangle_\xi$ decreasing linearly with r in the inner region (figure 4*d*). The profiles of $\langle n \rangle_\xi(r)$ and $\langle |\omega| \rangle_\xi(r)$ for both types of vortices

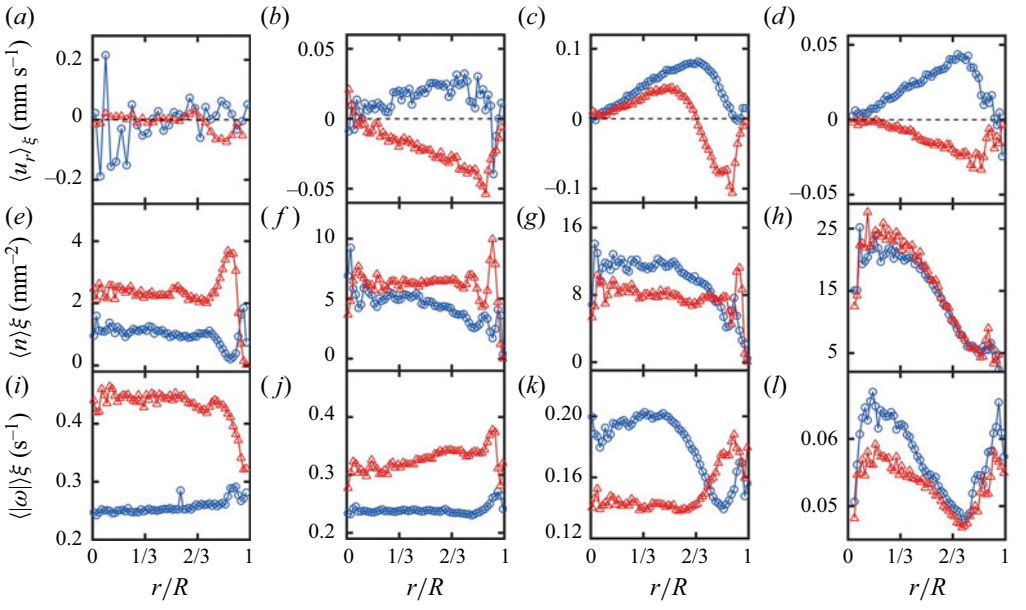

Figure 4. Plots of (*a–d*) ensemble-averaged radial velocity $\langle u_r\rangle_\xi$, (*e–h*) vortex density $\langle n\rangle_\xi$, and (*i–l*) vorticity amplitude $\langle|\omega|\rangle_\xi$ as functions of r/R, where $\langle\rangle_\xi$ denotes the ensemble average. Results are for $Ra = 2.0 \times 10^7$ with (*a*,*e*,*i*) $Ra/Ra_c = 54.8$ and $Fr = 0.030$, (*b*,*f*,*j*) $Ra/Ra_c = 4.57$ and $Fr = 0.044$, (*c*,*g*,*k*) $Ra/Ra_c = 2.26$ and $Fr = 0.12$, and (*d*,*h*,*l*) $Ra/Ra_c = 1.43$ and $Fr = 0.24$. Red triangles (blue circles) denote cyclonic (anticyclonic) data.

show similar radial dependence, suggesting that the symmetry of the vorticity field restores near the onset of convection.

We further investigate the parameter regime in which the inverse-centrifugal motion of cyclones occurs. We define the region boundary r_c for anomalous vortex motion as the mean radial velocity of cyclones $\langle u_r\rangle_\xi \geq 0$ for $r \leq r_c$, and $\langle u_r\rangle_\xi < 0$ for $r > r_c$. As shown in figure 4(*c*), r_c is thus the second zero crossing of the radial profile $\langle u_r\rangle_\xi(r)$. Figure 5(*a*) shows r_c/R as a function of Ra/Ra_c. We find $r_c = 0$ for $Ra/Ra_c \geq 4$, and r_c exceeds zero when Ra/Ra_c decreases below 4, reaching a peak at $Ra/Ra_c \approx 2$. With further decreasing in Ra/Ra_c, we see that r_c decreases, and the experimental data indicate the trend that r_c eventually approaches zero near the onset of convection $Ra/Ra_c \approx 1$. Near onset, our numerical data show a higher value of r_c than the experimental one, presumably owing to the insufficient numerical data evaluating the velocity profile $\langle u_r\rangle_\xi(r)$. Otherwise, results of r_c/R for various Ra collapse approximately onto one single curve. We calculate in the central region ($r \leq 0.5R$) the ratios of the number density γ_n and the vorticity magnitude γ_ω of the anticyclones over the cyclones. Figures 5(*b*) and 5(*c*) present results of γ_n and γ_ω as functions of Ra/Ra_c, respectively. We see that data of γ_n and γ_ω for various Ra also exhibit similar dependence of Ra/Ra_c. For $Ra/Ra_c > 10$, γ_n and γ_ω are constants irrespective of Ra/Ra_c, while γ_n and γ_ω increase when $Ra/Ra_c \leq 10$, and have a maximum at $Ra/Ra_c \approx 2$. When $Ra/Ra_c < 2$, the two ratios γ_n and γ_ω decrease with further decreasing Ra/Ra_c, and approach unity at the onset of convection.

The observed asymmetry of the vorticity field in the anomalous regime is attributed to the centrifugal effect. As the centrifugal force drives continuously hot (cold) fluid parcels towards (away from) the centre of the convection cell, the background fluid temperature in the central region increases and exceeds global mean fluid temperature (Hart & Olsen

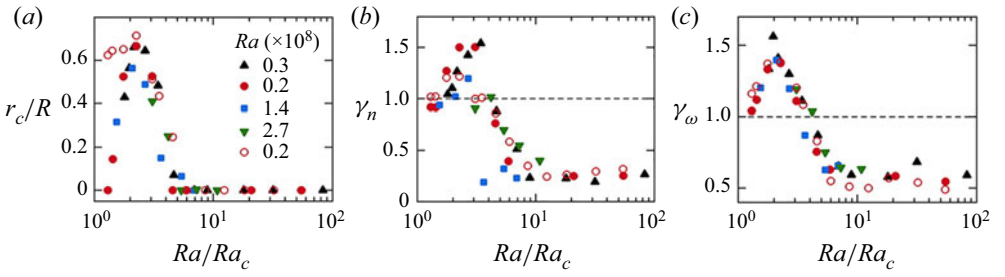

Figure 5. (*a*) The region boundary r_c/R for the inverse-centrifugal motion of cyclones. (*b*) The ratio γ_n of the number density of anticyclones over cyclones. (*c*) The ratio γ_ω of vorticity amplitude of anticyclones over cyclones. Results are shown as functions of Ra/Ra_c. Data for $Ra = 2.0 \times 10^7$ and $\Gamma_a = 3.8$ (circles), $Ra = 3.0 \times 10^7$ and $\Gamma_a = 3.8$ (up-triangles), $Ra = 1.4 \times 10^8$ and $\Gamma_a = 2.0$ (squares), and $Ra = 2.7 \times 10^8$ and $\Gamma_a = 2.0$ (down-triangles). The open circles are numerical data.

1999; Liu & Ecke 2011; Horn & Aurnou 2019). Thus in the central region, the temperature difference of the cold anticyclones from the background fluid becomes greater than that of the warm cyclones. Since such a temperature anomaly is proportional to the buoyancy forcing on the vortices, it is positively correlated to the vorticity magnitude of the vortices (Portegies *et al.* 2008; Grooms *et al.* 2010). It is also believed that the fluid warming in the central region enhances the stability of the anticyclonic flows, leading to a larger population of anticyclones. As a result, we find in figures 5(*b*) and 5(*c*) that both the number density and the vorticity magnitude of the anticyclones exceed the cyclonic values.

The aforementioned vortex dynamics and symmetric properties of the vorticity field reveal four distinct flow regimes depending on the rotation rates. (I) A randomly diffusive regime in the slow rotating limit, with Ra being one order in magnitude larger than Ra_c. In this flow regime, the vortices move in a random manner, yielding $\langle u_r \rangle_\xi \approx 0$, and r_c/R is close to zero. Since at the measured fluid height the cyclones have a greater population as well as a larger vorticity magnitude than the anticyclones, γ_n and γ_ω are both less than unity but independent of Ra/Ra_c. (II) A centrifugation-influenced regime ($4 \leq Ra/Ra_c \lesssim 10$) where the magnitude of $\langle u_r \rangle_\xi$ increases linearly with r (figure 4*b*). We observe that warm cyclones (cold anticyclones) move radially inwards (outwards), which is in agreement with the centrifugal effect. (III) An inverse-centrifugal regime ($1.6 \leq Ra/Ra_c \leq 4$) in which the cyclones exhibit anomalous outward motion in the inner region with $r \leq r_c$ (figure 4*c*). In this flow regime, anticyclones become the dominant flow structures in the sense that both γ_n and γ_ω greatly exceed unity (figures 5*b*,*c*). In the outer region ($r \geq r_c$), the centrifugal effect of fluid warming becomes insignificant, and we observe their inward cyclonic motion, as $\langle u_r \rangle_\xi$ for cyclones decreases with increasing r and becomes negative. (IV) The asymptotic regime in the rapid rotation limit ($Ra/Ra_c < 1.6$), where r_c approaches zero and the opposite radial motions of cyclones and anticyclones recover (figure 4*h*).

6. Vortex centrifugal motion

6.1. *Formation of vortex clusters*

We have seen that in the inverse-centrifugal regime, the symmetry of the vorticity field is broken, with the anticyclonic vortices dominating the cyclones in both strength and population. We show below that in this regime, the vortices self-organize into clusters in

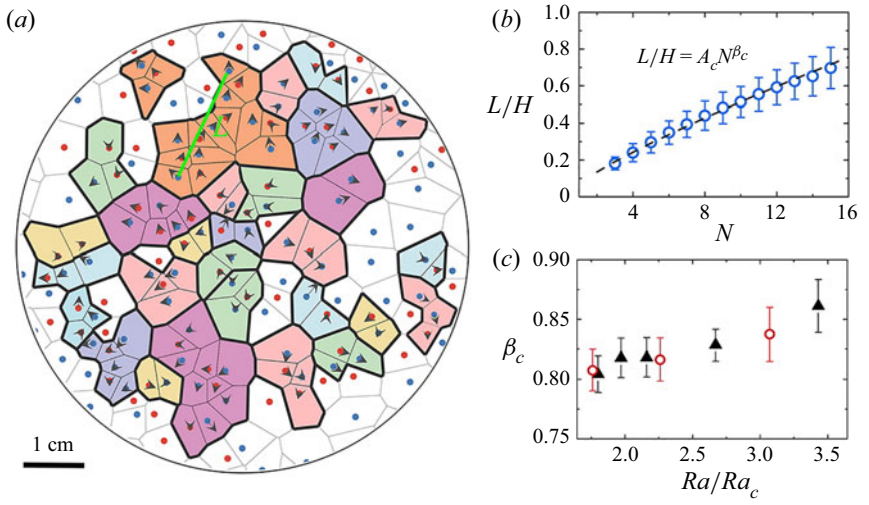

Figure 6. (*a*) Spatial distribution of vortex clusters. The polygons represent the Voronoi tessellations of the vortex centres. Voronoi cells within the same vortex cluster are presented in the same colour and enclosed by thick lines. The blue (red) dots denote the centroids of anticyclonic (cyclonic) vortices, with arrows indicating their velocity direction. Experimental data in a region $r \leq 0.7R$ are shown. (*b*) The normalized cluster length L/H as a function of cluster size N. The dashed line represents the fitted power function $L/H = A_c N^{\beta_c}$, where $A_c = 0.079$ and $\beta_c = 0.81$. Data in (*a*,*b*) are for $Ra = 3.0 \times 10^7$ and $Ra/Ra_c = 1.97$. (*c*) The exponent β_c as a function of Ra/Ra_c for various Ra. Open circles: $Ra = 2.0 \times 10^7$. Solid triangles: $Ra = 3.0 \times 10^7$.

which the anticyclones dominate the long-range correlated vortex motion, leading to the inverse-centrifugal motion of the cyclones.

Figure 6(*a*) presents an example of instantaneous spatial distribution and motion of the vortices in the inverse-centrifugal regime. We find that the adjacent vortices often move in similar directions and aggregate locally, forming vortex clusters. Here, we adopt the following two criteria to identify vortex clusters (see e.g. Chen *et al.* 2012):

(1) the distance between two neighbouring vortices is smaller than 1.5 times the mean vortex diameter;
(2) the angle between the velocity of two adjacent vortices is less than θ^*.

Our analysis over the range $30^\circ \leq \theta^* \leq 75^\circ$ confirms that the results of correlated vortex motion are not sensitive to the choice of θ^*. In the following, we discuss statistical properties using $\theta^* = 60^\circ$.

In figure 6(*a*), vortex clusters are identified using the aforementioned criteria. In this Voronoi diagram of vortex centres, each cluster is enclosed by thick lines, with Voronoi cells within the same cluster presented in the same colour. We define the cluster length L as the largest distance between two vortex centres within the cluster, and compute the number of vortices N with each cluster. Figure 6(*b*) shows L as a function of N for $Ra = 3 \times 10^7$ and $Ra/Ra_c = 1.97$. We find that $L(N)$ can be well fitted by a power function $L = A_c N^{\beta_c}$. Assuming that the distance between two adjacent vortices d_{vv} is independent of N, the power exponent β_c then reveals the dimensional properties of clusters. When $\beta_c = 0.5$, vortices in a cluster are distributed isotropically in a two-dimensional plane. When $\beta_c = 1$, vortices line up to form one-dimensional clusters. Figure 6(*c*) shows that within the full parameter range of Ra/Ra_c studied, β_c increases slightly from 0.80 to 0.87 with increasing Ra/Ra_c, suggesting a fractal property of the vortex clusters: vortices in a cluster have

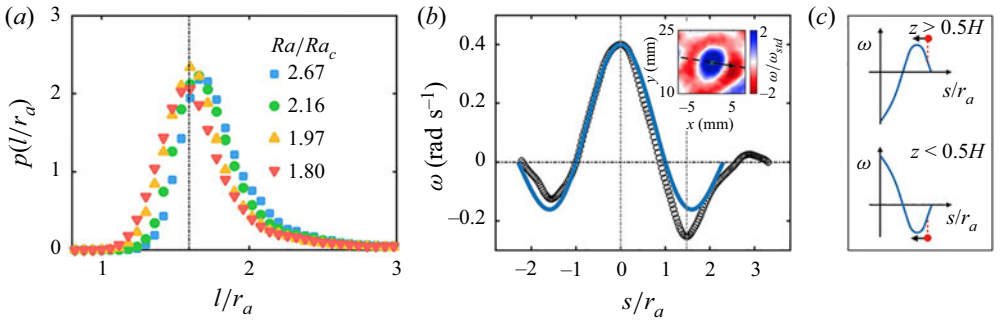

Figure 7. (*a*) The PDFs of the distance l between an anticyclone and its neighbouring cyclones within a cluster, normalized by the radius of the anticyclone r_a. The vertical dashed line shows a maximum $p(l/r_a)$ at $l = l_m = cr_a$. (*b*) Vorticity profile $\omega(s/r_a)$ of an opposite-signed vortex pair along the centreline s. The anticyclonic radius r_a is defined by the radial position where $\omega(s/r_a)$ crosses zero. Open circles: experimental data. Solid line: the scaled zero-order Bessel functions $J_0(k_s/r_a)\omega(0)/J_0(0)$, where $k = 2.405$ is the first zero of J_0. The two vertical dashed lines indicate the centres of the anticyclone and the cyclone at $s_1 = 0$ and $s_2 = cr_a$. The inset shows the vorticity distribution of this vortex pair, with the dashed line being the centreline. (*c*) Schematic plot of the interaction between a pair of opposite-signed convective columnar vortices at the upper layer (top) and lower layer (bottom). The blue curve represents the vorticity profile of a downwelling vortex, which creates a background vorticity field that influences the motion of an adjacent upwelling vortex (denoted by the red circle). Data are for $Ra = 3.0 \times 10^7$ and $Fr = 0.27$.

a weak preference to be arranged along one direction, while the horizontal span of the cluster is not isotropic but dependent on the orientation.

Within each cluster, the vortices exhibit long-range correlated motions. We attribute these correlated vortex motions to the vortex–vortex interaction that occurs in a convection state where the vortices are distributed densely. Figure 7(*a*) shows the PDF $p(l/r_a)$ of the distance l between a downwelling vortex (anticyclone when observed in the lower half fluid layer) and its neighbouring upwelling vortices for various Ra/Ra_c. Here, r_a is the radius of the downwelling vortex. One sees that $p(l)$ has an apparent maximum at $l_m = cr_a = 1.593r_a$. Here, the constant c is the ratio of the first minimum to the first zero of the zero-order Bessel function J_0. Since $p(l)$ represents the probability of finding upwelling vortices at a distance l from a downwelling vortex, it reflects the interactions between adjacent counter-rotating vortices. Figure 7(*b*) shows an example of the vorticity profile $\omega(s)$ of two opposite-signed neighbouring vortices, with the coordinate s measuring the distance to the centre of the downwelling vortex along the connecting line. We see that within the core region ($s < l_m$), the vorticity profile $\omega(s)$ is well described by $J_0(s)$, and $\omega(s)$ reaches a first minimum at $s = l_m$, where $p(l)$ is maximum. Such a pairwise vorticity profile is commonly observed within vortex clusters in our experiment.

We provide the following interpretation for the most probable vortex separation l_m. We consider the motion of warm, upwelling vortices in the vicinity of a cold, downwelling vortex. Observed in the lower half fluid layer ($z < H/2$), the cold vortex gives rise to a negative background vorticity gradient in the core region ($s < l_m$), but a positive vorticity gradient outside the vortex core ($s > l_m$) (see a schematic drawing in figure 7*c*). The theory of vortex motion on a vorticity gradient (Schecter & Dubin 1999) suggests that an upwelling vortex, which possesses negative vorticity in the lower half-layer in our case, moves down the vorticity gradient due to the background shear flow. Thus inside the core region ($s < l_m$), the upwelling vortex moves away from the downwelling vortex centre, but moves towards it when $s > l_m$. Since a vortex with positive vorticity moves up

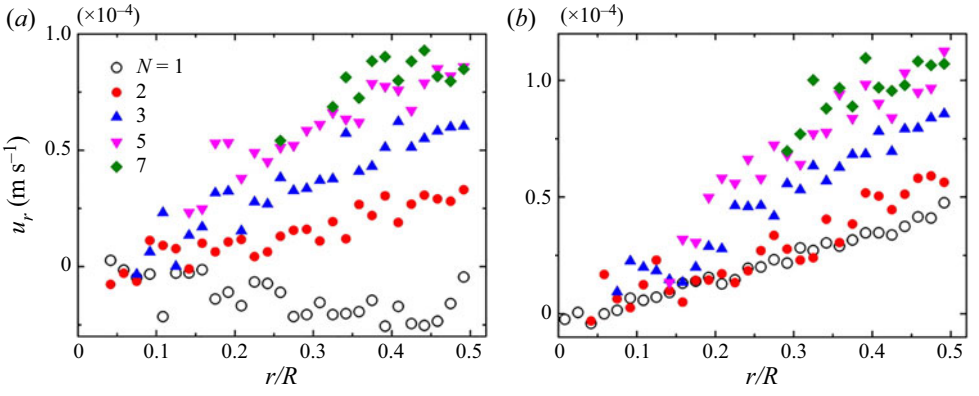

Figure 8. Ensemble-averaged radial velocity $\langle u_r \rangle_\xi$ of the vortices as a function of r/R for various cluster sizes N. Data are for (a) cyclones and (b) anticyclones. Results for $Ra = 2.0 \times 10^7$ and $Ra/Ra_c = 2.26$.

a background vorticity gradient, the upwelling vortex undergoes the same translational motions in the upper half-layer. As a result, we find $s = l_m$ to be the most probable radial position where an upwelling vortex is located as shown in figure 7(a). For the same reason, one finds most probably a downwelling vortex at a radial distance $s = cr_c$ from an upwelling vortex centre (with r_c being the radius of the upwelling vortex). Therefore, we conclude that two opposite-signed convective columnar vortices have a trend of forming a stable pair and exhibit correlated motions.

6.2. *Centrifugal motion of clustered vortices*

We have shown that it is the interaction between adjacent opposite-signed vortices that organizes individual vortices to form vortex clusters. Within each vortex cluster, the translational motion of the vortices is closely correlated and restricted with each other. In the following, we make comparative studies of the radial motions of clustered vortices (inside clusters) and isolated vortices (outside clusters).

Figure 8 shows the ensemble-averaged radial velocity $\langle u_r \rangle_\xi$ for the vortices in clusters with various sizes N. For isolated cyclones that move individually (i.e. $N = 1$), $\langle u_r \rangle_\xi$ is negative and its magnitude increases approximately linearly with r, indicating the normal inward motion of cyclones. However, for clustered cyclones ($N \geq 2$), $\langle u_r \rangle_\xi$ becomes positive, which implies anomalous outward motion. We see that the slope of $\langle u_r \rangle_\xi(r)$ increases when N increases up to 5. Therefore, clustered cyclones gain a larger velocity of inverse-centrifugal motion when the cluster size increases. The velocity profile of anticyclones exhibits a cluster size dependence similar to that of the cyclones, except that for $N = 1$, $\langle u_r \rangle_\xi(r)$ is positive, since isolated anticyclones move outwardly.

We determine the slope λ_u of the velocity profile through fitting the data $\langle u_r \rangle_\xi$ in the region $0 \leq r \leq 0.5R$ using (5.1). Results for λ_u as a function of cluster size N for $Ra/Ra_c = 2.67$ are shown in figure 9(a). We see clearly that in this inverse-centrifugal regime, λ_u for cyclones changes sign when N exceeds 1. Data for both types of vortices suggest a similar trend for $N \geq 2$, i.e. λ_u increases with N for small cluster sizes and reaches a maximum at $N = 5$. We also note that for small cluster size, λ_u is considerably larger for anticyclones than for cyclones.

When vortices inside a cluster move collectively, they share a similar radial velocity profile $\langle u_r \rangle_\xi(r)$. It is thus reasonable to consider all vortices inside the cluster as a single

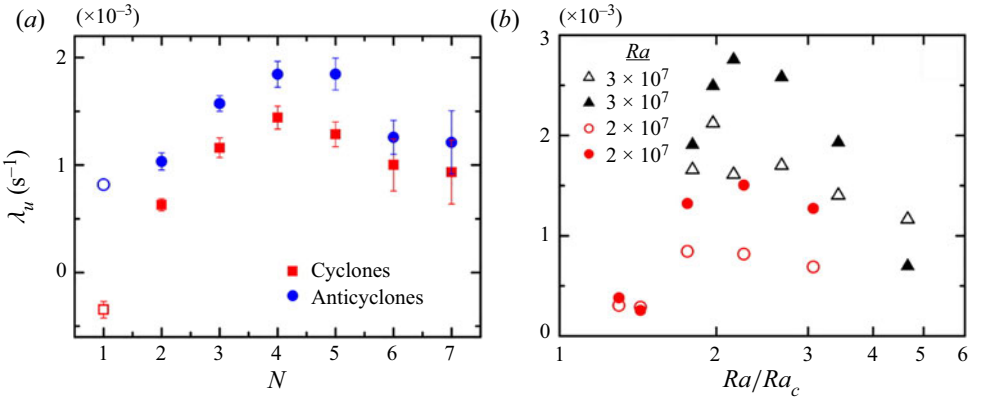

Figure 9. Mobility λ_u of vortex motion determined from the slope of $\langle u_r \rangle_\xi(r)$: (*a*) λ_u as a function of N for $Ra = 2.0 \times 10^7$ and $Ra/Ra_c = 2.26$; (*b*) λ_u as a function of Ra/Ra_c for various Ra. Open symbols are data for isolated anticyclones ($N = 1$). Solid symbols are data for clustered anticyclones ($N > 1$).

structure that undergoes radial motion driven by the centrifugal force. Here, we interpret the radial motion of vortex clusters using a Langevin-type equation analogous to (1.2) in § 1 (see also discussions in Ding *et al.* 2021). For a given initial radial position of a cluster, its radial mobility is given by $\lambda_u \approx |1/(2t_c) - \sqrt{1/(4t_c^2) + \zeta}|$, where the relaxation time $t_c = M/\eta$ for the cluster's motion is given by the inertia mass M of all vortices inside the cluster, η is the dynamic viscosity, $\zeta = \Omega^2 \langle \delta T \rangle$ is the coefficient of the net centrifugal force for all clustered vortices, and $\langle \delta T \rangle$ is the averaged temperature anomaly of the vortex cluster. Since in the inverse-centrifugal regime both the population and vorticity strength of anticyclones overrides that of cyclones, the net centrifugal force is positive, thus the vortex cluster moves outwardly.

As shown in figure 9(*a*), the mobility of clusters λ_u is in the order of $10^{-3}\,\mathrm{s}^{-1}$, and $t_c \approx 10\,\mathrm{s}$ in the inverse-centrifugal regime (see Ding *et al.* 2021); we find $1/(2t_c) \gg \lambda_u$, $\zeta \ll 1/(2t_c)^2$, thus $\lambda_u \approx \zeta t_c = \Omega^2 \langle \delta T \rangle M/\eta$. With increasing cluster size N, the inertia mass M of the cluster increases. We suggest that it is the dominating factor for an enlarged λ_u for clusters of intermediate size ($N \approx 5$). For very large cluster sizes ($N \geq 5$), we infer that viscous damping may become significant to influence cluster motion, and thereby λ_u decreases.

Figure 9(*b*) presents λ_u as a function of Ra/Ra_c for isolated ($N = 1$, open symbols) and clustered ($N > 1$, solid symbols) anticyclones. Data for two sets of Ra are shown for comparison. One sees that for a given Ra and Ra/Ra_c, λ_u is greater for clustered anticyclones than for isolated anticyclones. For all cases, λ_u has a maximum at $Ra/Ra_c \approx 2$. We see that the maximum λ_u for clustered anticyclones is nearly twice that of the isolated ones for both Ra numbers. We also see that λ_u increases further when a larger Ra is chosen. These results demonstrate that the radial motion of anticyclones is enhanced by the collective motion to a great extent.

6.3. *Froude number dependence of the vortex mobility*

The mobility λ_u represents the primary features of radial motion for both isolated and clustered vortices. We suggest that the non-monotonic dependence of λ_u on Ra/Ra_c shown in figure 9(*b*) is thus owing to the decreasing vorticity magnitude $|\omega|$ that competes with the increasing rotation rate Ω. Following discussions in § 6.2, we have

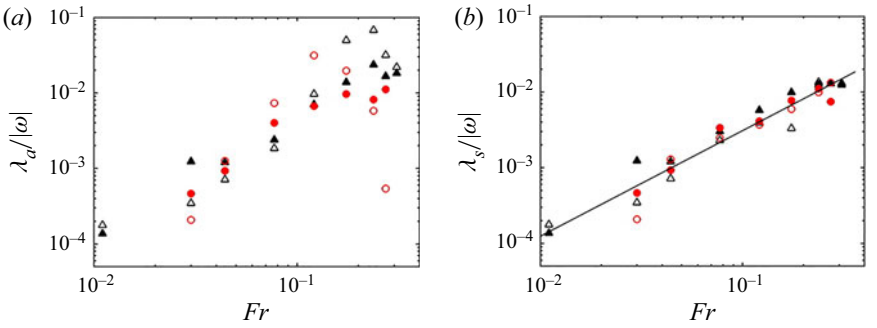

Figure 10. (*a*) The mobility $\lambda_a/|\omega|$ of all vortices scaled by the vorticity magnitude as a function of Fr. (*b*) The scaled mobility $\lambda_s/|\omega|$ of isolated vortices as a function of Fr. Results are for $Ra = 2.0 \times 10^7$ (red circles) and $Ra = 3.0 \times 10^7$ (black triangles). Open symbols: cyclones. Solid symbols: anticyclones. The solid line represents a power-function fit with exponent 1.40 ± 0.13.

$\lambda_u \approx \zeta t_c = \Omega^2 \delta T\, m/\eta$. The temperature anomaly δT of the convective vortices represents the buoyancy forcing, which is predicted to be proportional to the vorticity magnitude of the vortices (Portegies *et al.* 2008; Grooms *et al.* 2010). Thus the mobility of clusters can approximate to $\lambda_u \approx c^*(z)\Omega^2\,|\omega|\,m/\eta$, with the coefficient $c^*(z)$ depending on the fluid depth. This approximate relation implies that the mobility of the vortices is determined not only by the rotating rate but also by the vorticity magnitude of the vortices.

In figure 10, we show the scaled mobility $\lambda_a/|\omega|$ as a function of Fr for both types of vortices. Here, λ_a is determined by linear fitting of the radial velocity profile $\langle u_r\rangle_\xi(r)$ shown in figure 9 for both isolated ($N = 1$) and clustered ($N > 1$) vortices. Since $\lambda_a/|\omega| = c^*(z)\,\Omega^2 m/\eta$, the scaled mobility is expected to increase when the rotation rate increases. Our experimental results in figure 9(*a*) show that this is the case, as $\lambda_a/|\omega|$ for both cyclones and anticyclones grows rapidly with increasing Fr in the full parameter range studied. Meanwhile, we see that results for $\lambda_a/|\omega|$ are scattered, and there exists a notable difference between the cyclonic and anticyclonic data for given Fr and Ra.

We suggest that the vortex interaction of vortices forming clusters may disturb individual vortex motion and modify the vortex mobility. In support of this argument, we determine the mobility λ_s for isolated vortices, calculating the slope of the velocity profile $\langle u_r\rangle_\xi(r)$ (e.g. shown in figure 9) for both cyclones and anticyclones for the case of $N = 1$. Results for $\lambda_s/|\omega|$ are shown as a function of Fr in figure 10(*b*). We see that the discrepancy of $\lambda_s/|\omega|$ between isolated cyclones and anticyclones is minor. Moreover, data for $\lambda_s/|\omega|$ for various Ra collapse onto a power-law function $\lambda_s/|\omega| \propto Fr^{1.40\pm0.13}$ in the full parameter range of Fr studied, suggesting a general scaling relationship. These results imply that the mobility of isolated vortices scaled by the magnitude of their vorticity can be determined adequately by the Froude number.

7. Vortex lifespan

Observations of the evolution of vortex structures suggest that the generation and disappearance of the vortices occur seemingly randomly in time. In this section, we present the statistical analysis of the lifespan of vortices. We calculate the number $N(t)$ of vortices that have a lifespan longer than time t. Figure 11 shows the results for $N(t)/N_0$ as a function of time for various Ra/Ra_c. Here, N_0 is the number of all vortices observed over the course of the experiment. We see that for both types of vortices, $N(t)/N_0$ decreases exponentially

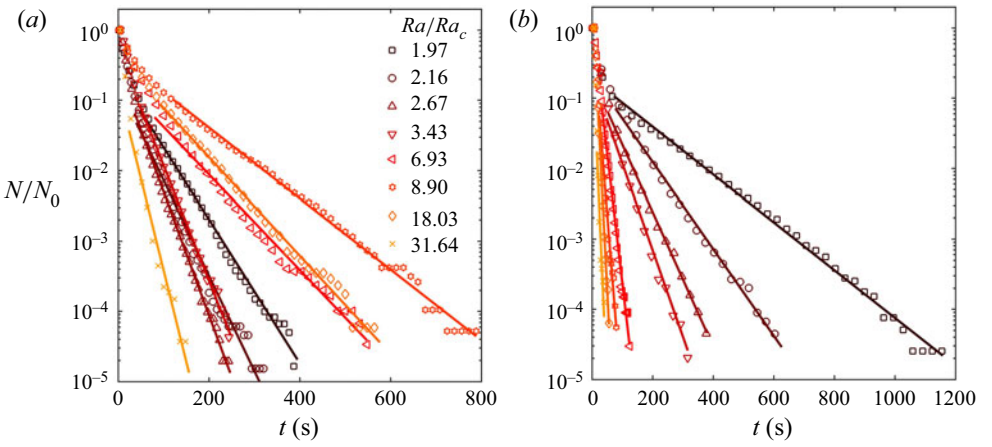

Figure 11. Results of $N(t)/N_0$ as a function of time for (*a*) cyclones and (*b*) anticyclones, for $Ra = 3.0 \times 10^7$. The solid curves represent the fitted exponential function $N(t)/N_0 = A\exp(-t/\tau)$.

in large time limits. The solid lines in figure 11 represent the fitted exponential functions to the data, that is, $N(t)/N_0 = A\exp(-t/\tau)$, with τ being the characteristic lifespan of the vortices, and A a fitting coefficient. The exponential decay law of $N(t)$ in figure 11 can be understood considering that each vortex has a constant disappearing probability p in unit time. The decreasing rate is expected to be proportional to the number of existent vortices, i.e. $\mathrm{d}N/\mathrm{d}t = -pN$. This simple model leads to the exponential decay law for $N(t)$, and yields the characteristic vortex lifespan $\tau = 1/p$ of the long-lived vortices.

Meanwhile, we notice that in a short time ($t \ll \tau$), $N(t)$ decays faster than the fitted exponential curves, as shown in figure 11, suggesting that short-lifespan vortices may die out with a higher probability. It could be that a subset of these vortices arises from vortex interactions or background turbulence, and exhibits distinct behaviour of evolution compared to the long-lived, coherent vortices. Nevertheless, these short-lifespan vortices have little influence on the statistical properties of the vortex lifespan τ.

The characteristic lifespan τ for both types of vortices at different Ra/Ra_c is shown in figure 12. For a given Ra, the lifespan of anticyclones shows a clear increasing trend with decreasing Ra/Ra_c (figure 12*a*). The lifespan of cyclones, however, exhibits a non-monotonic dependence on Ra/Ra_c. Figure 12(*b*) shows that a local minimum of τ appears within the inverse-centrifugal regime $1.6 \leq Ra/Ra_c \leq 4$, which is attributed to the fact that cyclones undergo the normal inward motion in the outer region ($r > r_c$), but are forced to move outwardly in the inner region ($r < r_c$) owing to the vortex clustering effect (see figure 5*c*). The convergent radial motion of the cyclones results in a relatively short lifespan τ on average, maintaining a constant vortex number density as observed in the experiment.

To compare the lifespan of the two types of vortices, we show in figure 12(*c*), as a function of Ra/Ra_c, the ratio γ_τ of the lifespan of anticyclones over the cyclones. We see that the lifespan of anticyclones is around one order of magnitude shorter than that of cyclones in the flow regime (I) (when $Ra/Ra_c \geq 10$). As Ra/Ra_c decreases below 10, γ_τ increases. When the system enters into the inverse-centrifugal regime (III) ($Ra/Ra_c \leq 4$), the lifespan of anticyclones starts to override that of cyclones. The remarkable similarity in the Ra/Ra_c dependence of γ_τ, γ_n and γ_ω (see figures 5*b*,*c*) suggests that the vortex lifespan is strongly influenced by the centrifugal effects.

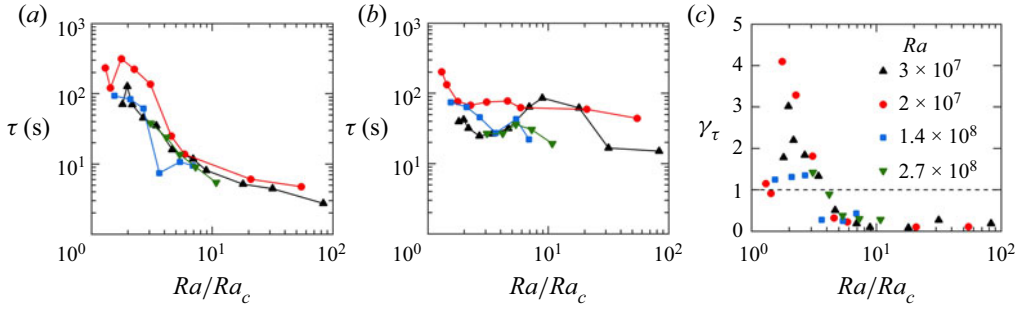

Figure 12. The characteristic lifespan τ of (*a*) anticyclones and (*b*) cyclones, as a function of Ra/Ra_c. (*c*) The ratio γ_τ of the lifespan of anticyclones to that of cyclones, as a function of Ra/Ra_c.

We examine the radial dependence of the vortex lifespan in flow regimes where the radial motion of vortices is prominent. Here, we calculate the number $N_{r0}(t)$ of vortices that arise at an initial radial position $r_0 \pm 0.05R$ and have a lifespan larger than t. Figures 13(*a*) and 13(*b*) show N_{r0}/N_0 as a function of time for cyclones and anticyclones, respectively, for various r_0, with N_0 being a normalization coefficient. Here, N_{r0}/N_0 appears to depend sensitively on the initial radial position r_0, and for each r_0, N_{r0}/N_0 follows persistently the exponential decay in time. In figures 13(*c*) and 13(*d*), we show results of the lifespan τ as a function of r_0 for two types of vortices. It is notable that τ depends sensitively on the initial location for $Ra/Ra_c = 2.67$, while in the centrifugation-influenced regime ($Ra/Ra_c = 4.66$), τ appears relatively constant with varying r_0. In the inverse-centrifugal regime ($Ra/Ra_c = 2.67$), the lifespan of cyclones decreases with increasing r_0 in the inner region ($r \lesssim r_c$), reaching a minimum at the region boundary ($r_0 \approx r_c$), followed by an increase in the outer region ($r \gtrsim r_c$). Hence cyclones around the boundary of the inverse-centrifugal region have the shortest lifespan. For anticyclones, τ decreases monotonically with r_0. These results also reveal that vortices generated within the inner region ($r_0 < r_c$) possess in general a longer lifespan than vortices generated in the outer region. We suggest two reasons that may be responsible for vortices in the inner region having longer lifespans. First, since vortex clusters form mostly in the inner region (see figure 6*a*), they have larger inertia and are more stable against perturbations from the background turbulent flows, which stabilizes the structure of the vortices within. Second, annihilation and merging events of adjacent vortices occur less frequently within clusters as the clustered vortices are moving in a collective manner.

8. Summary and discussions

A major emphasis of previous studies in rotating convection has been on the flow structures of the convective vortices in rotating RBC (Vorobieff & Ecke 2002; Sprague *et al.* 2006; Portegies *et al.* 2008; Grooms *et al.* 2010; Nieves *et al.* 2014; Rajaei *et al.* 2017; Shi *et al.* 2020) and partly on their stochastic translational motions (Sakai 1997; King & Aurnou 2012; Noto *et al.* 2019; Chong *et al.* 2020; Ding *et al.* 2021). We investigate here their spatial distribution, lifespan and radial motion in the parameter ranges $2.0 \times 10^7 \leq Ra \leq 2.7 \times 10^8$, $1.7 \times 10^{-5} \leq Ek \leq 2.7 \times 10^{-4}$ and $1.2 \times 10^{-3} \leq Fr \leq 0.31$, which cover four flow regimes of vortex motion: (I) random vortex diffusion, (II) centrifugal-forced radial motion, (III) inverse-centrifugal motion, and (IV) asymptotic centrifugal motion. We report that under slow rotations with $Ra \gtrsim 10\,Ra_c$, the vortices undergo Brownian-type random motion, i.e. the mean square displacement (MSD) of the vortices increases first

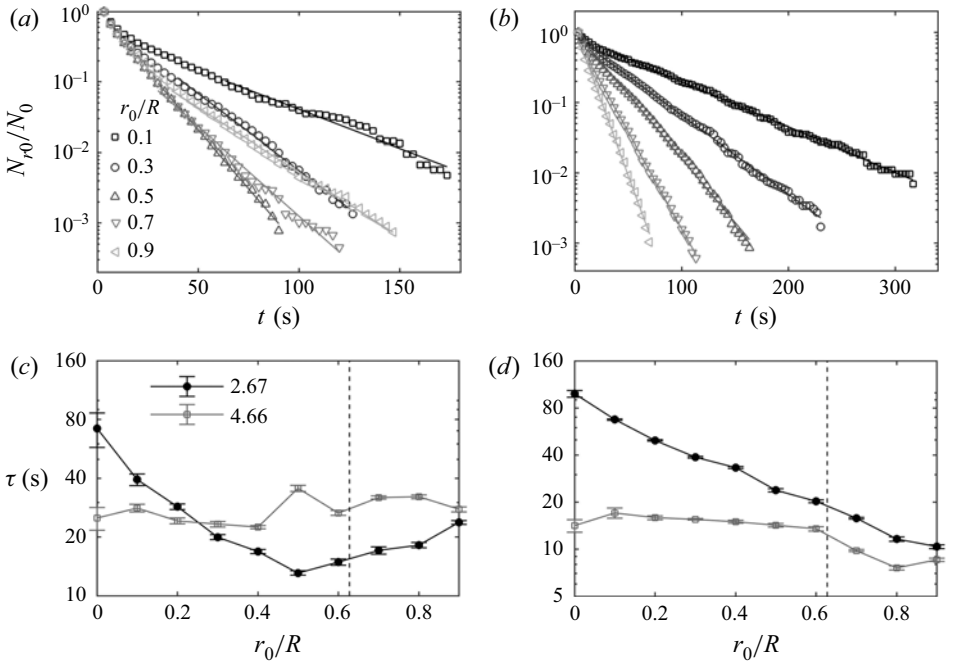

Figure 13. Results for N_{r0}/N_0 as a function of time for (a) cyclones and (b) anticyclones arising at various initial radial positions. Data are for $Ra/Ra_c = 2.67$, $Ra = 3 \times 10^7$. The characteristic lifespan τ of (c) cyclones and (d) anticyclones as a function of r_0/R for two sets of Ra/Ra_c. Solid symbols: $Ra/Ra_c = 2.67$. Open symbols: $Ra/Ra_c = 4.66$. The vertical dashed lines denote the inverse-centrifugal region boundary $r_0 = r_c$ for $Ra/Ra_c = 2.67$.

in time as t^2 in the ballistic regime, and then linearly in the diffusive regime. Our close inspection of the PDFs of the vortex displacements reveals that, however, the ballistic motion of the vortices is non-Gaussian at small time intervals. Furthermore, we show that in the limit of slow rotations ($Ra \approx 80\,Ra_c$), the vortices are randomly distributed over the horizontal plane, with the PDFs of the Voronoi cell areas of the vortices well described by the standard Γ distribution.

With modest strength of rotations, the centrifugal force influences the dynamics of the vortices. We observed that in this flow regime with $4\,Ra_c \leq Ra \leq 10\,Ra_c$, cyclones move radially towards the rotation axis, while anticyclones migrate outwards. Thus the MSD of the vortices increases faster than a linear function of time at a large time. Moreover, we note that the ensemble average of the radial velocity $\langle u_r \rangle_\xi$ of cyclones (anticyclones) is negative (positive) and decreases (increases) linearly with respect to r. The centrifugal motion of the vortices in a background of turbulent fluctuation can be interpreted through an extended Langevin model incorporating centrifugal acceleration. In this flow regime, we find that the horizontal scale of the vortices, and thus the mean area A of vortex Voronoi cells, decreases with increasing rotating rate. The size distribution of the Voronoi cells deviates from the standard Γ distribution, as reflected by the decreasing of their standard deviation $\sigma(A/\langle A \rangle)$.

Under rapid rotations with $1.6\,Ra_c \leq Ra \leq 4\,Ra_c$, the mean area of the Voronoi cells of the vortices decreases significantly, signifying that the vortices are distributed densely. In this convection state, the hydrodynamic interaction of neighbouring vortices becomes

prominent to influence the vortex dynamics. We report the existence of a most probable separation between two adjacent counter-rotating vortices that tend to form a vortex pair and move collectively. Such vortex interactions eventually lead to the formation of large-scale vortex clusters. As a result, the size of the vortex Voronoi cells becomes diversified, thus $\sigma(A/\langle A\rangle)$ increases with decreasing Ra/Ra_c. In this flow regime, the cold anticyclones override the warm cyclones in vorticity strength, population and lifespan, a flow field asymmetry brought about by the centrifugal effect. Within vortex clusters, the motion of the weak cyclones thus submits to that of strong anticyclones and moves outwardly in a collective manner. Within each vortex cluster, the translational motion of the vortices is long-range correlated. We show that such correlated motion of the clustered vortices exerts essential influences on their dynamics. With increasing cluster size N, the radial velocity $\langle u_r\rangle_\xi(r)$ for clustered cyclones and anticyclones increases faster with r, thus both types of vortices gain a larger translation velocity moving outwardly. Despite the complicated Fr dependence of the scale vortex mobility $\lambda_a/|\omega|$ for all vortices, we discover in the full parameter range of Fr a simple power-law scaling $\lambda_s/|\omega| \propto Fr^{1.4}$ for isolated vortices for various Ra and vortex types.

Finally, an intriguing aspect of rotating convection systems is the lifespan τ of the coherent vortices. We report that the number of vortices $N(t)$ with a lifespan exceeding t decays exponentially in time. Such an exponential decay law suggests that the convective vortices experience a constant rate $1/\tau$ of disappearance (e.g. through merging or annihilation events). The fact that spatial- and time-averaged vortex number density n remains constant implies that the convective vortices are generated with constant rate $1/\tau$. Our studies of the statistical properties of the vortex lifespan may provide valuable insights into the evaluation of the vortex distributions and dynamics in rotating convection.

We have shown in this work the rich and intriguing vortex dynamics in rotating RBC. There remain numerous issues requiring further investigations. Prominent among those is the origin of the Brownian but non-Gaussian diffusion of the vortex displacements. Such non-Gaussian diffusive motion becomes apparent at short time scales. Another crucial issue awaiting theoretical descriptions is the hydrodynamic interactions among closely located convective vortices that give rise to the long-range collective motion of the vortices. What are the implications of the vortex dynamics presented in this study for the correlated vortex motion observed in giant gaseous planets and other large-scale geophysical and astrophysical flows (Li *et al.* 2020; Gavriel & Kaspi 2021, 2022; Mura *et al.* 2021)? We expect future progress in answering these questions.

Funding. This work is supported by the National Science Foundation of China under grant nos 92152105, 12232010 and 12072144, by an NSFC/RGC Joint Research Grant no. 11561161004 (J.-Q.Z.) and N_CUHK437/15 (K.-Q.X.), and by the Hong Kong Research Grants Council under grant nos 14301115 and 14302317. J.-Q.Z. acknowledges support from the Research Program of Science and Technology Commission of Shanghai Municipality.

Declaration of interests. The authors report no conflict of interest.

Author ORCIDs.
Shan-Shan Ding https://orcid.org/0000-0001-9673-1294;
Guang-Yu Ding https://orcid.org/0000-0001-8636-9738;
Kai Leong Chong https://orcid.org/0000-0002-3182-368;
Ke-Qing Xia https://orcid.org/0000-0001-5093-9014;
Jin-Qiang Zhong https://orcid.org/0000-0001-8368-2120.

Author contributions. J.-Q.Z. and K.-Q.X. conceived and designed the research. S.-S.D. and W.-T.W. conducted the experiments. G.-Y.D. and K.L.C conducted the numerical simulations. S.-S.D., J.-Q.Z. and K.-Q.X. wrote the paper.

References

Aurnou, J.M., Bertin, V. & Grannan, A.M. 2018 Rotating thermal convection in liquid gallium: multi-modal flow, absent steady columns. *J. Fluid Mech.* **846**, 846–876.

Boubnov, B.M. & Golitsyn, G.S. 1986 Experimental study of convective structures in rotating fluids. *J. Fluid Mech.* **167**, 503–531.

Chandrasekhar, S. 1961 *Hydrodynamic and Hydromagnetic Stability*. Oxford University Press.

Chen, X., Dong, X., Be'er, A., Swinney, H.L. & Zhang, H.P. 2012 Scale-invariant correlations in dynamic bacterial clusters. *Phys. Rev. Lett.* **108** (14), 148101.

Chong, K.L., Ding, G. & Xia, K.-Q. 2018 Multiple-resolution scheme in finite-volume code for active or passive scalar turbulence. *J. Comput. Phys.* **375**, 1045–1058.

Chong, K.L., Shi, J.-Q., Ding, S.-S., Ding, G.-Y., Lu, H.-Y., Zhong, J.-Q. & Xia, K.-Q. 2020 Vortices as Brownian particles in turbulent flows. *Sci. Adv.* **6**, eaaz1110.

Ding, S.-S., Chong, K.L., Shi, J.-Q., Ding, G.-Y., Lu, H.-Y., Xia, K.-Q. & Zhong, J.-Q. 2021 Inverse centrifugal effect induced by collective motion of vortices in rotating turbulent convection. *Nat. Commun.* **12**, 5585.

Ding, S.-S., Zhang, H.-L., Chen, D.-T. & Zhong, J.-Q. 2022 Vortex patterns in rapidly rotating Rayleigh–Bénard convection under spatial periodic forcing. *J. Fluid Mech.* **950**, R1.

Ferenc, J.-S. & Néda, Z. 2007 On the size distribution of Poisson Voronoi cells. *Physica* A **385** (2), 518–526.

Fernando, H.J.S. & Smith, D.C. 2001 Vortex structures in geophysical convection. *Eur. J. Mech.* B/*Fluids* **20**, 437–470.

Fujita, K., Tasaka, Y., Yanagisawa, T., Noto, D. & Murai, Y. 2020 Three-dimensional visualization of columnar vortices in rotating Rayleigh–Bénard convection. *J. Vis.* **24**, 635–647.

Gascard, J.-C., Watson, A.J., Messias, M.-J., Olsson, K.A., Johannessen, T. & Simonsen, K. 2002 Long-lived vortices as a mode of deep ventilation in the Greenland Sea. *Nature* **416**, 525–527.

Gavriel, N. & Kaspi, Y. 2021 The number and location of Jupiter's circumpolar cyclones explained by vorticity dynamics. *Nat. Geosci.* **14**, 559–563.

Gavriel, N. & Kaspi, Y. 2022 The oscillatory motion of Jupiter's polar cyclones results from vorticity dynamics. *Geophys. Res. Lett.* **49**, e2022GL098708.

Grooms, I., Julien, K., Weiss, J.B. & Knobloch, E. 2010 Model of convective Taylor columns in rotating Rayleigh–Bénard convection. *Phys. Rev. Lett.* **104**, 224501.

Hart, J.E. & Olsen, D.R. 1999 On the thermal offset in turbulent rotating convection. *Phys. Fluids* **11**, 2101–2107.

Hopfinger, E.J. & van Heijst, G.J.F. 1993 Vortices in rotating fluids. *Annu. Rev. Fluid Mech.* **25**, 241–289.

Horn, S. & Aurnou, J.M. 2019 Rotating convection with centrifugal buoyancy: numerical predictions for laboratory experiments. *Phys. Rev. Fluids* **4**, 073501.

Hu, Y.-B., Huang, S.-D., Xie, Y.-C. & Xia, K.-Q. 2021 Centrifugal-force-induced flow bifurcations in turbulent thermal convection. *Phys. Rev. Lett.* **127**, 244501.

Jones, C.A. 2011 Planetary magnetic fields and fluid dynamos. *Annu. Rev. Fluid Mech.* **43**, 583–614.

Julien, K. & Knobloch, E. 1998 Strongly nonlinear convection cells in a rapidly rotating fluid layer: the tilted f-plane. *J. Fluid Mech.* **360**, 141–178.

Julien, K., Legg, S., McWilliams, J. & Werne, J. 1996 Rapidly rotating Rayleigh–Bénard convection. *J. Fluid Mech.* **322**, 243–273.

Julien, K., Rubio, A.M., Grooms, I. & Knobloch, E. 2012 Statistical and physical balances in low Rossby number Rayleigh–Bénard convection. *Geophys. Astrophys. Fluid Dyn.* **106**, 392–428.

Kaczorowski, M. & Xia, K.-Q. 2013 Turbulent flow in the bulk of Rayleigh–Bénard convection: small-scale properties in a cubic cell. *J. Fluid Mech.* **722**, 596–617.

King, E.M. & Aurnou, J.M. 2012 Thermal evidence for Taylor columns in turbulent rotating Rayleigh–Bénard convection. *Phys. Rev.* E **85**, 016313.

King, E.M., Stellmach, S., Noir, J., Hansen, U. & Aurnou, J.M. 2009 Boundary layer control of rotating convection systems. *Nature* **457**, 301.

Kundu, P.K. & Cohen, I.M. 2008 *Fluid Mechanics*. Academic Press.

Kunnen, R.P.J. 2021 The geostrophic regime of rapidly rotating turbulent convection. *J. Turbul.* **22** (4–5), 267–296.

KUNNEN, R.P.J., CLERCX, H.J.H. & GEURTS, B.J. 2010 Vortex statistics in turbulent rotating convection. *Phys. Rev.* E **82**, 036306.

LI, C., INGERSOLL, A.P., KLIPFEL, A.P. & BRETTLE, H. 2020 Modeling the stability of polygonal patterns of vortices at the poles of Jupiter as revealed by the Juno spacecraft. *Proc. Natl Acad. Sci. USA* **117**, 24082–24087.

LIU, Y. & ECKE, R.E. 2011 Local temperature measurements in turbulent rotating Rayleigh–Bénard convection. *Phys. Rev.* E **84**, 016311.

LU, H.-Y., DING, G.-Y., SHI, J.-Q., XIA, K.-Q. & ZHONG, J.-Q. 2021 Heat-transport scaling and transition in geostrophic rotating convection with varying aspect ratio. *Phys. Rev. Fluids* **6** (7), L071501.

MARSHALL, J. & SCOTT, F. 1999 Open-ocean convection: observations, theory, and models. *Rev. Geophys.* **37**, 1–64.

MURA, A., *et al.* 2021 Oscillations and stability of the Jupiter polar cyclones. *Geophys. Res. Lett.* **48**, e2021GL094235.

NIEVES, D., RUBIO, A.M. & JULIEN, K. 2014 Statistical classification of flow morphology in rapidly rotating Rayleigh–Bénard convection. *Phys. Fluids* **26**, 086602.

NIILER, P.P. & BISSHOPP, F.E. 1965 On the influence of Coriolis force on onset of thermal convection. *J. Fluid Mech.* **22**, 753–761.

NOTO, D., TASAKA, Y., YANAGISAWA, T. & MURAI, Y. 2019 Horizontal diffusive motion of columnar vortices in rotating Rayleigh–Bénard convection. *J. Fluid Mech.* **871**, 401.

PORTEGIES, J.W., KUNNEN, R.P.J., VAN HEIJST, G.J.F. & MOLENAAR, J. 2008 A model for vortical plumes in rotating convection. *Phys. Fluids* **20**, 066602.

RAJAEI, H., KUNNEN, R.P.J. & CLERCX, H.J.H. 2017 Exploring the geostrophic regime of rapidly rotating convection with experiments. *Phys. Fluids* **20**, 045105.

SAKAI, S. 1997 The horizontal scale of rotating convection in the geostrophic regime. *J. Fluid Mech.* **333**, 85–95.

SCHECTER, D.A. & DUBIN, D.H. 1999 Vortex motion driven by a background vorticity gradient. *Phys. Rev. Lett.* **83**, 2191–2194.

SHI, J.-Q., LU, H.-Y., DING, S.-S. & ZHONG, J.-Q. 2020 Fine vortex structure and flow transition to the geostrophic regime in rotating Rayleigh–Bénard convection. *Phys. Rev. Fluids* **5**, 011501(R).

SPRAGUE, M., JULIEN, K., KNOBLOCH, E. & WERNE, J. 2006 Numerical simulation of an asymptotically reduced system for rotationally constrained convection. *J. Fluid Mech.* **551**, 141–174.

STELLMACH, S., LISCHPER, M., JULIEN, K., VASIL, G., CHENG, J.S., RIBEIRO, A., KING, E.M. & AURNOU, J.M. 2014 Approaching the asymptotic regime of rapidly rotating convection: boundary layers versus interior dynamics. *Phys. Rev. Lett.* **113**, 254501.

TAGAWA, Y., MERCADO, J.M., PRAKASH, V.N., CALZAVARINI, E., SUN, C. & LOHSE, D. 2012 Three-dimensional Lagrangian Voronoï analysis for clustering of particles and bubbles in turbulence. *J. Fluid Mech.* **693**, 201–215.

VALLIS, G.K. 2006 *Atmospheric and Oceanic Fluid Dynamics*. Cambridge University Press.

VOROBIEFF, P. & ECKE, R.E. 1998 Vortex structure in rotating Rayleigh–Bénard convection. *J. Fluid Mech.* **123**, 156–160.

VOROBIEFF, P. & ECKE, R.E. 2002 Turbulent rotating convection: an experimental study. *J. Fluid Mech.* **458**, 191–218.

WESTERWEEL, J., ELSINGA, G.E. & ADRIAN, R.J. 2013 Particle image velocimetry for complex and turbulent flows. *Annu. Rev. Fluid Mech.* **45**, 409–436.

DE WIT, X.M., AGUIRRE GUZMÁN, A.J., MADONIA, M., CHENG, J.S., CLERCX, H.J.H. & KUNNEN, R.P.J. 2020 Turbulent rotating convection confined in a slender cylinder: the sidewall circulation. *Phys. Rev. Fluids* **5**, 023502.

ZHANG, X., VAN GILS, D.P.M., HORN, S., WEDI, M., ZWIRNER, L., AHLERS, G., ECKE, R.E., WEISS, S., BODENSCHATZ, E. & SHISHKINA, O. 2020 Boundary zonal flow in rotating turbulent Rayleigh–Bénard convection. *Phys. Rev. Lett.* **124**, 084505.

ZHONG, F., ECKE, R. & STEINBERG, V. 1993 Rotating Rayleigh–Bénard convection: asymmetric modes and vortex states. *J. Fluid Mech.* **249**, 135.